



## Open Archive Toulouse Archive Ouverte



OATAO is an open access repository that collects the work of Toulouse researchers and makes it freely available over the web where possible

This is an author's version published in: <http://oatao.univ-toulouse.fr/22088>

### Official URL:

<https://doi.org/10.1109/TUFFC.2017.2731627>

### To cite this version:

Kim, Jonghoon and Mamou, Jonathan and Hill, Paul and Canagarajah, Nishan and Kouamé, Denis  and Basarab, Adrian  and Achim, Alin *Approximate message passing reconstruction of quantitative acoustic microscopy images*. (2018) IEEE Transactions on Ultrasonics, Ferroelectrics and Frequency Control, 65 (3). 327-338. ISSN 0885-3010 .

Any correspondence concerning this service should be sent to the repository administrator: [tech-oatao@listes-diff.inp-toulouse.fr](mailto:tech-oatao@listes-diff.inp-toulouse.fr)

# Approximate Message Passing Reconstruction of Quantitative Acoustic Microscopy Images

Jonghoon Kim, Jonathan Mamou, *Senior Member, IEEE*, Paul R. Hill, *Member, IEEE*,  
Nishan Canagarajah, Denis Kouamé, *Member, IEEE*, Adrian Basarab, *Member, IEEE*,  
and Alin Achim, *Senior Member, IEEE*

**Abstract**—A novel framework for compressive sensing (CS) data acquisition and reconstruction in quantitative acoustic microscopy (QAM) is presented. Three different CS patterns, adapted to the specifics of QAM systems, were investigated as an alternative to the current raster-scanning approach. They consist of diagonal sampling, a row random, and a spiral scanning pattern and can all significantly reduce both the acquisition time and the amount of sampled data. For subsequent image reconstruction, we design and implement an innovative technique, whereby a recently proposed approximate message passing method is adapted to account for the underlying data statistics. A Cauchy maximum a posteriori image denoising algorithm is thus employed to account for the non-Gaussianity of QAM wavelet coefficients. The proposed methods were tested retrospectively on experimental data acquired with a 250- or 500-MHz QAM system. The experimental data were obtained from a human lymph node sample (250 MHz) and human cornea (500 MHz). Reconstruction results showed that the best performance is obtained using a spiral sensing pattern combined with the Cauchy denoiser in the wavelet domain. The spiral sensing matrix reduced the number of spatial samples by a factor of 2 and led to an excellent peak signal-to-noise ratio of 43.21 dB when reconstructing QAM speed-of-sound images of a human lymph node. These results demonstrate that the CS approach could significantly improve scanning time, while reducing costs of future QAM systems.

**Index Terms**—Approximate message passing (AMP), Cauchy distribution, compressive sensing (CS), quantitative acoustic microscopy (QAM).

## I. INTRODUCTION

ALTHOUGH introduced more than 30 years ago, quantitative acoustic microscopy (QAM) is still a “new” imaging technology employed to investigate soft biological tissue at microscopic resolution by eliciting its mechanical property when irradiated with very high frequency ultrasound [1]. Specifically, by processing RF echo data, QAM yields 2-D quantitative maps of the acoustical and mechanical properties of soft tissues (e.g., speed of sound, acoustic impedance, and acoustic attenuation). Therefore, QAM provides a novel

contrast mechanism compared to histology photomicrographs and optical and electron microscopy images [4]. To date, our group and others have successfully used QAM to investigate a wide range of soft biological tissues such as liver samples, lymph nodes, retina, and even living cells [1]–[5]. Several of these recent studies were performed using QAM systems equipped with spherically focused single-element transducers having center frequencies of 250 or 500 MHz, which yielded 2-D maps of acoustic properties with spatial resolutions of 7 and 4  $\mu\text{m}$ , respectively [2], [3]. Currently, QAM requires a complete 2-D raster scan of the sample to form images, thus yielding a large amount of RF data when using a conventional spatial sampling scheme (e.g., 2 and 1  $\mu\text{m}$  steps at 250 and 500 MHz, respectively). Likewise, sonography techniques exploiting ultrasound need to acquire a considerable amount of data (thus significantly exceeding the Nyquist rate) in order to perform high-resolution digital beamforming. Therefore, compressive sensing (CS) has been intensively studied as a breakthrough to overcome the limitation of contemporary technology [13].

From this perspective, this paper presents a novel approach to improve the efficiency of QAM RF data acquisition and reconstruction by developing a dedicated CS scheme.

Traditionally, statistical signal processing has been centered in its formulation on the hypotheses of Gaussianity and stationarity. This is justified by the central limit theorem and leads to classical least square approaches for solving various estimation problems. The introduction of various sparsifying transforms starting with the penultimate decade of the last century, together with the adoption of various statistical models that are able to model various degrees of non-Gaussianity and heavy-tails, have led to a progressive paradigm shift [7]. At the core of modern signal processing methodology sits the concept of sparsity. The key idea is that many naturally occurring signals and images can be faithfully reconstructed from a lower number of transform coefficients than the original number of samples (i.e., acquired according to Nyquist theorem) [8]. In this sense, CS could prove to be a powerful solution to decrease the amount of data in QAM and to accelerate the acquisition process at potentially no cost to image quality. In terms of reconstruction, most CS methods rely on  $l_1$ -norm minimization using a linear programming algorithm [31]. All these approaches do not exploit the true statistical distribution of the data and are motivated by the inability of the classical least-squares approach to estimate the reconstructed signal.

Manuscript received April 5, 2017; accepted July 18, 2017. Date of publication July 21, 2017; date of current version March 1, 2018. The work of D. Kouame and A. Basarab was supported in part by CIMI Labex, Toulouse, France, under Grant ANR-11-LABX-0040-CIMI and Program ANR-11-IDEX-0002-02. (Adrian Basarab and Alin Achim are shared last authors.) (Corresponding author: Alin Achim.)

J. Kim, P. R. Hill, N. Canagarajah, and A. Achim are with the Visual Information Laboratory, Merchant Venturers School of Engineering, University of Bristol, Bristol BS8 1UB, U.K. (e-mail: alin.achim@bristol.ac.uk).

J. Mamou is with the Frederic L. Lizzi Center for Biomedical Engineering, Riverside Research, New York, NY 10038 USA.

D. Kouamé and A. Basarab are with the IRIT UMR CNRS 5505, University of Toulouse, CNRS, INPT, UPS, UT1C, UT2J, 31062 Toulouse, France.

Digital Object Identifier 10.1109/TUFFC.2017.2731627

In this paper, an approximate-message-passing-(AMP)-based algorithm was designed to reconstruct QAM images from spatially undersampled measurements. AMP is a simplified version of message passing derived from belief propagation in graphical models [9] and is characterized not only by dramatically reduced convergence times but also by a reconstruction performance equivalent to  $l_p$ -based methods. AMP uses an iterative process consisting of a sparse-representation based image denoising algorithm performed at each iteration [28]. Hence, selection of a robust denoiser and of the most efficient sparsifying basis are essential issues to address in order to achieve fast convergence and high recovery quality [10]. Our proposed AMP-based QAM imaging framework consists of the following two major modules.

- 1) In the data acquisition component of our system, we propose novel techniques for QAM data sampling, by choosing sensing matrices that simultaneously meet CS requirements and take into account the peculiarities of practical QAM acquisition devices, instead of.
- 2) In the image reconstruction component, we design and test a wavelet domain AMP-based approach, which exploits underlying data statistics through the use of a Cauchy-based *maximum a posteriori* (MAP) algorithm.<sup>1</sup>

This paper is structured as follows. Section II covers the essential, necessary background on QAM, CS, and AMP. Section III introduces the main theoretical contributions of this paper. Specifically, in Section III-A, we present the derivation of the wavelet-based Cauchy denoiser. In Section III-B, we describe three different sensing patterns for QAM. Section IV compares the performance of our proposed method with that of the existing CS reconstruction techniques, including previously proposed AMP algorithms. Finally, conclusions and future work directions are detailed in Section V.

## II. THEORETICAL BACKGROUND

### A. Quantitative Acoustic Microscopy

In QAM, a high-frequency (e.g., >50 MHz), single-element, spherically focused (e.g., F-number < 1.3) transducer transmits a short ultrasound pulse and receives the RF echo signals reflected from the sample that consists of a thin section of soft tissue affixed to a microscopy slide (Fig. 1). The echo RF data are composed of two main reflections (see  $S_1$  and  $S_2$  in Fig. 1):  $S_1$  originates from the interface between the coupling medium (degassed saline) and the specimen and  $S_2$  from the interface between the specimen and the glass substrate interface as illustrated in Fig. 1. At each scan location, the RF data are digitized, saved, and processed offline to yield values of speed of sound ( $c$ ), acoustic impedance ( $z$ ), and attenuation ( $\alpha$ ) [14]. Signal processing also requires the use of a reference signal obtained from a region devoid of sample ( $S_0$  in Fig. 1). Briefly, the ratio of the Fourier transform of a sample signal,  $S$  and  $S_0$ , is computed and fit to a forward model to estimate the time of flight differences between  $S_1$  and  $S_0$  and  $S_2$  and  $S_0$ . These time differences are used to estimate  $c$  in the sample as well as the tissue thickness (i.e.,

<sup>1</sup>An initial version of this algorithm was presented in [11], but the work therein was focused on natural images.

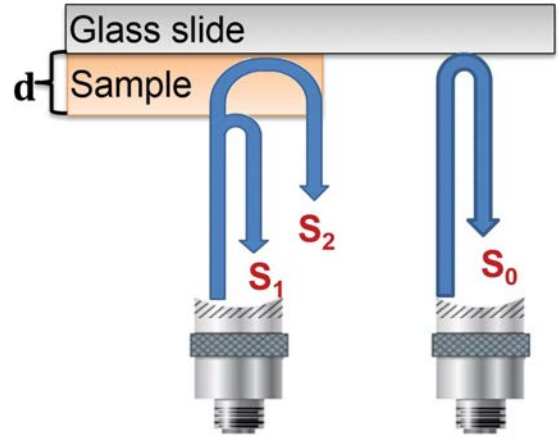


Fig. 1. Illustrative working principle of QAM. RF data from the above sample location is composed of two reflections, while RF data from the above glass slide is composed of only one reflection. Many QAM systems operate in the so-called upside-down configuration, because holding the transducer from the top usually generates too much vibration at the tip of transducer creating blurring artifact in the reconstructed QAM images.

$d$  in Fig. 1) at that location. The forward model fit also provides the amplitude of  $S_1$ , which is used to estimate  $z$  of the sample. Finally, the amplitude of  $S_2$ , its frequency dependence, and the previously estimated tissue thickness are used to estimate  $\alpha$  [14]. The transducer is raster scanned and the values obtained at each scan location are then combined to form quantitative 2-D parameter maps. Fig. 2 shows the working principle of QAM as well as the 500-MHz QAM system used in this paper (Fig. 1), namely the transducer and the thin sample affixed to a microscopy slide. Samples are obtained from fixed or frozen samples sectioned using a microtome or a cryotome. In the case of fixed samples, the paraffin is removed and the sample is rehydrated before imaging. In the case of frozen samples, the sample is thawed and rehydrated before imaging. These protocols are common and used in histopathology. Following QAM data acquisition, the samples can be stained and imaged using optical microscopy approaches, and histology photomicrographs can easily be co-registered with QAM images. Therefore, successfully applying a CS approach to QAM acquisition could significantly reduce the amount of RF data recorded compared to conventional raster scanning without significantly degrading the quantitative 2-D maps of acoustic properties. In this paper, a new CS scheme is proposed for QAM, and to test it, it was applied retrospectively to decimated 2-D quantitative maps directly.

### B. Compressive Sensing

CS is based on measuring a significantly reduced number of samples than what is dictated by the Nyquist theorem. Given a correlated image, the traditional transform-based compression method performs the following steps: 1) acquires all  $N$  samples of the signal; 2) computes a complete set of transform coefficients (e.g., discrete cosine transform or wavelet); and 3) selectively quantizes and encodes only the  $K \ll N$  most significant coefficients. This procedure is highly inefficient, because a significant proportion of the output of the analog-

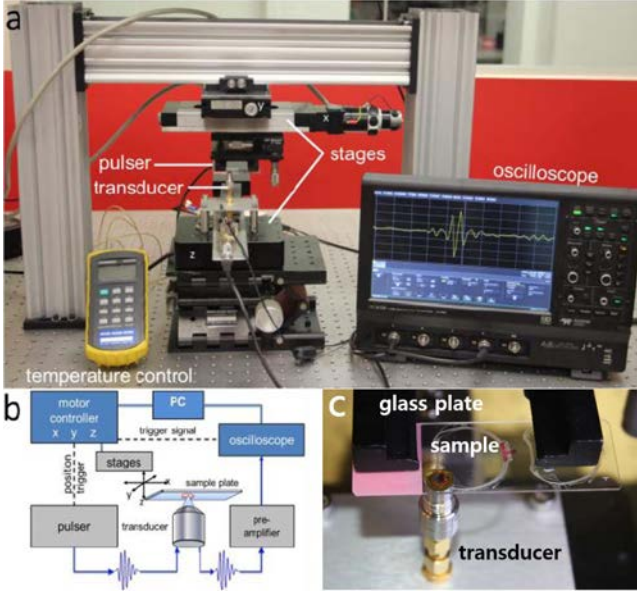


Fig. 2. (a) Photograph of the 500-MHz QAM system. (b) Block diagram of working principle. (c) Magnification of sample mounting and transducer. An eye sample from eye bank is visible on the microscopy glass slide. Our QAM system does not currently employ a temperature controller; rather, we measure the coupling fluid temperature at the beginning and the end of the scanning, linearly interpolate between the two values, and use these values to estimate a speed of sound in water at each location. Typically, the variation of temperature is less than 0.5 °C.

to-digital conversion process ends up being discarded. CS is concerned with sampling signals more parsimoniously, acquiring only the relevant signal information, rather than sampling followed by compression. The main hallmark of this methodology is that, given a compressible signal, a small number of linear projections, directly acquired before sampling, contain sufficient information to effectively perform the processing of interest (such as signal reconstruction, detection, and classification). In terms of signal approximation, Candès *et al.* [8] and Donoho [16] have demonstrated that if a signal is  $K$ -sparse in one basis (meaning that the signal is exactly or approximately represented by  $K$  elements of this basis), then it can be recovered from  $M = \text{cst} \cdot K \cdot \log(N/K) \ll N$  fixed (nonadaptive) linear projections onto a second basis, called the measurement basis, which is incoherent with the sparsity basis [33], and where  $\text{cst} > 1$  is a small overmeasuring constant. The CS measurement model is

$$\mathbf{y} = \Phi \mathbf{x} + \mathbf{n} \quad (1)$$

where  $\mathbf{y} \in \mathbb{R}^M$  is the measurement vector,  $\mathbf{x} \in \mathbb{R}^N$  is the signal to be reconstructed,  $\Phi \in \mathbb{R}^{M \times N}$  is the measurement matrix, and  $\mathbf{n} \in \mathbb{R}^M$  is an additive white Gaussian noise.

In terms of reconstruction, using the  $M$  measurements in the first basis and given the  $K$ -sparsity property in the other basis, the original signal can be recovered by taking a number of different approaches. The majority of these approaches solve constrained optimization problems. Commonly used approaches are based on convex relaxation (basis pursuit [8]), nonconvex optimization (reweighted  $l_p$  minimization [17]), or greedy strategies (orthogonal matching pursuit [18]). As another

alternative, iterative thresholding approaches to CS recovery problem have attracted significant interest, owing to faster reconstruction than what can be achieved by convex optimization. Blumensath and Davies [19] and Donoho [20] proved that correct solution could be obtained via soft or hard thresholding of observations measured from sparse signals.

### C. Approximate Message Passing Reconstruction

In the context of CS, AMP reconstructs an original image from a reduced number of linear measurements by performing elementwise denoising at each iteration. Indeed, the AMP algorithm can be interpreted as recursively solving an image denoising problem. Specifically, at each AMP iteration, one observes a noise perturbed original image. Reconstructing the image amounts to successive noise cancellations until the noise variance decreases to a satisfactory level. The algorithm can be succinctly summarized mathematically through the following two steps:

$$\mathbf{x}^{t+1} = \eta_t(\Phi^T \mathbf{z}^t + \mathbf{x}^t) \quad (2)$$

$$\mathbf{z}^t = \mathbf{y} - \Phi \mathbf{x}^t + \frac{1}{\delta} \mathbf{z}^{t-1} \langle \eta'_{t-1}(\Phi^T \mathbf{z}^{t-1} + \mathbf{x}^{t-1}) \rangle \quad (3)$$

where  $\mathbf{x}$ ,  $\mathbf{y}$ ,  $\mathbf{z}$ , and  $\delta$  denote a sparse signal, observation, residual, and undersampling ratio ( $M/N$ ), respectively.  $\eta(\cdot)$  is a function that represents the denoiser,  $\eta'(\cdot)$  is its first derivative, and  $\langle \mathbf{x} \rangle = (1/N) \sum_{i=1}^N (x_i)$ . The superscript  $t$  represents the iteration number and  $(\cdot)^T$  is the classical conjugate transpose notation. Given  $\mathbf{x} = \mathbf{0}$  and  $\mathbf{z} = \mathbf{y}$  as an initial condition, the algorithm iterates sequentially (2) and (3) until satisfying a stopping criterion or reaching a preset iteration number. The last term of the right-hand side in (3) is referred to as the Onsager reaction term and is also acknowledged to contribute to balancing the sparsity-undersampling tradeoff [9], [21].

An extended wavelet-based AMP system can be generated by integrating a wavelet transform (denoted by  $W$ ) into (2) and (3) using the following transformation:

$$\mathbf{y} = \Phi \underbrace{W^{-1} \theta_{\mathbf{x}}}_{\mathbf{x}} + \mathbf{n} \quad (4)$$

where  $W^{-1}$  denotes the inverse wavelet transform  $W$  and  $\theta_{\mathbf{x}}$  becomes the sparse representation of  $\mathbf{x}$  within wavelet domain. Introducing  $\Theta$  as the new notation for  $\Phi W^{-1}$ , we get the following expressions:

$$\theta_{\mathbf{x}}^{t+1} = \eta_t(\Theta^T \mathbf{z}^t + \theta_{\mathbf{x}}^t) \quad (5)$$

$$\mathbf{z}^t = \mathbf{y} - \Theta \theta_{\mathbf{x}}^t + \frac{1}{\delta} \mathbf{z}^{t-1} \langle \eta'_{t-1}(\Theta^T \mathbf{z}^{t-1} + \theta_{\mathbf{x}}^{t-1}) \rangle. \quad (6)$$

The subsequently defined denoising algorithms seek to denoise the elements of  $\theta_{\mathbf{q}}^t = \Theta^T \mathbf{z}^t + \theta_{\mathbf{x}}^t$  corresponding to the contaminated wavelet coefficients. To simplify the following notation, the  $i$ th element of  $\theta_{\mathbf{q}}^t$  is defined as  $\theta_{\mathbf{q},i}^t = v$  and the  $i$ th element of the denoised output  $\theta_{\mathbf{x}}^{t+1}$  is defined as  $\theta_{\mathbf{x},i}^{t+1} = \hat{w}$  (a denoised estimate of the true coefficient  $w$ ).

The most important design consideration is arguably the choice of the shrinkage (denoising) function  $\eta$  in (5). In the following, we introduce two previously defined functions [6], [21], which will be later used for comparison purpose within our experimental results in Section IV-A.

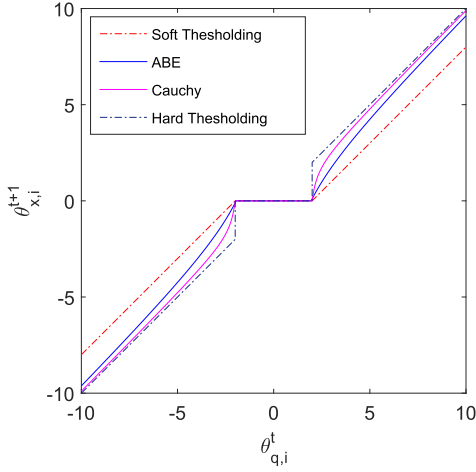


Fig. 3. Comparison of behavior among four different denoisers.

#### 1) Soft Threshold Denoiser:

$$\begin{aligned}\hat{w} &= \eta(v) = \text{sign}(v)(|v| - \tau) \cdot \mathbb{K}_{(|v| > \tau)} \\ \eta'(v) &= \mathbb{K}_{(|v| > \tau)}\end{aligned}\quad (7)$$

where  $\mathbb{K}(\cdot)$  is the indicator function. The threshold  $\tau$  is defined as the  $M$ th largest magnitude value of  $\theta_q^t$  [9].

#### 2) Amplitude-Scale-Invariant Bayes Estimator Denoiser:

$$\begin{aligned}\hat{w} &= \eta(v) = \frac{(v^2 - 3\sigma^2)_+}{v} \\ \eta'(v) &= \mathbb{K}_{(v^2 > 3\sigma^2)} \cdot \left(1 + 3\left(\frac{\sigma}{v}\right)^2\right)\end{aligned}\quad (8)$$

where  $\sigma^2$  is the noise variance at iteration  $t$  and  $(\cdot)_+$  is the right handed function where  $(u)_+ = 0$  if  $u \leq 0$  and  $(u)_+ = u$  if  $u > 0$ .

As far as the CS reconstruction of conventional ultrasound images is concerned, the denoiser in (8) was shown to achieve a better performance than iteratively reweighted least squares (IRLS) and  $l_p$  programming [29]. Therefore, we hypothesize that ABE should also be a successful criterion for QAM images; consequently, we shall use it for benchmarking our method. Fig. 3 illustrates the behavior of the denoising function for four different denoisers, of which ABE and the Cauchy-based denoisers that are introduced in the subsequent section can be regarded as a compromise between soft-thresholding and hard-thresholding [24]. The labels on the horizontal and vertical axes correspond to corrupted wavelet coefficient and their denoised version, respectively. Subscript  $i$  represents the index of each element, which implies element-wise denoising, as stated before.

### III. CAUCHY-AMP FOR COMPRESSED QAM IMAGING

This section describes the key features of wavelet-based Cauchy-AMP together with the practical sensing patterns as a novel approach for QAM CS reconstruction.

#### A. Wavelet-Based Cauchy-AMP

Wavelet coefficients provide a sparse representation for natural images [27]. In addition, they can be accurately modeled

using heavy tailed distributions [25], [26] such as the  $\alpha$ -stable distribution [22], [23]. The Cauchy distribution is a special case of the  $\alpha$ -stable family that not only has a heavy tailed form but also has a compact analytical probability density function given in [11]

$$P(w) = \frac{\gamma}{w^2 + \gamma^2} \quad (9)$$

where  $w$  and  $\gamma$  are the wavelet coefficient value and the dispersion parameter (controlling the spread of the distribution), respectively. Given (9), a MAP estimator method (10) can lead to the derivation of explicit formulae (14) estimating a clean wavelet coefficient  $w$  from an observed coefficient observation  $v$  contaminated with additive Gaussian noise (i.e.,  $n = v - w$  with noise variance  $\sigma^2$ ) [12]

$$\hat{w} = \arg \max_w P_{w|v}(w|v). \quad (10)$$

The posterior probability  $P_{w|v}(w|v)$  can be expressed, by Bayes' theorem, as

$$P_{w|v}(w|v) = \frac{P_{v|w}(v|w)P_w(w)}{P_v(v)}. \quad (11)$$

Assuming that  $P_{v|w}(v|w) \sim N(0, \sigma^2)$ , the logarithmic form of (10) is given in (12), which is mathematically more intuitive. The evidence  $P_v(v)$  is constant for all inputs and, therefore, can be ignored

$$\hat{w}(v) = \arg \max_w \left[ -\frac{(v-w)^2}{2\sigma^2} + \log \left( \frac{\gamma}{w^2 + \gamma^2} \right) \right]. \quad (12)$$

To find the solution to (12), take the first derivative of the terms in the bracket relative to  $w$  and set to zero

$$\hat{w}^3 - v\hat{w}^2 + (\gamma^2 + 2\sigma^2)\hat{w} - \gamma^2 v = 0. \quad (13)$$

Using Cardano's method, the estimate of  $w$  can be found in (14) of which the first derivative is (15)

$$\hat{w} = \eta(v) = \frac{v}{3} + s + t \quad (14)$$

$$\hat{w}' = \eta'(v) = 1/3 + s' + t' \quad (15)$$

where  $s$  and  $t$  are values determined by  $v$  and  $\sigma^2$  iteratively updated at each iteration together with a constant value  $\gamma$ ;  $\sigma^2$  is estimated as the variance of the  $\mathbf{z}$  vector defined in (6).  $s$  and  $t$  are defined as

$$\begin{aligned}s &= \sqrt[3]{\frac{q}{2} + dd}, \quad t = \sqrt[3]{\frac{q}{2} - dd} \\ dd &= \sqrt{p^3/27 + q^2/4} \\ p &= \gamma^2 + 2\sigma^2 - v^2/3 \\ q &= v\gamma^2 + 2v^3/27 - (\gamma^2 + 2\sigma^2)v/3.\end{aligned}\quad (16)$$

$s'$  and  $t'$  are found as follows:

$$\begin{aligned}s' &= \frac{q'/2 + dd'}{3(q/2 + dd)^{(2/3)}}, \quad t' = \frac{q'/2 - dd'}{3(q/2 - dd)^{(2/3)}} \\ dd' &= \frac{p'p^2/9 + q'q/2}{2dd} \\ p' &= -2v/3 \\ q' &= -2\sigma^2/3 + 2\gamma^2/3 + 2v^2/9.\end{aligned}\quad (17)$$

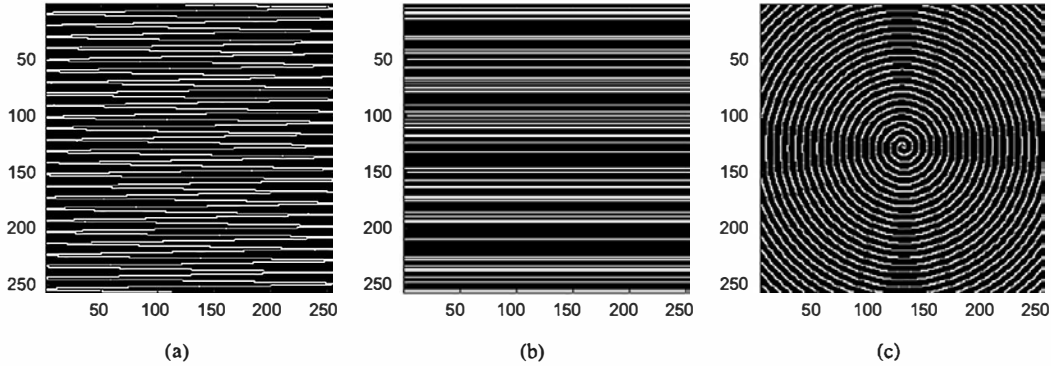


Fig. 4. Proposed three different types of sampling masks. (a) Diagonal. (b) Row random. (c) Spiral.

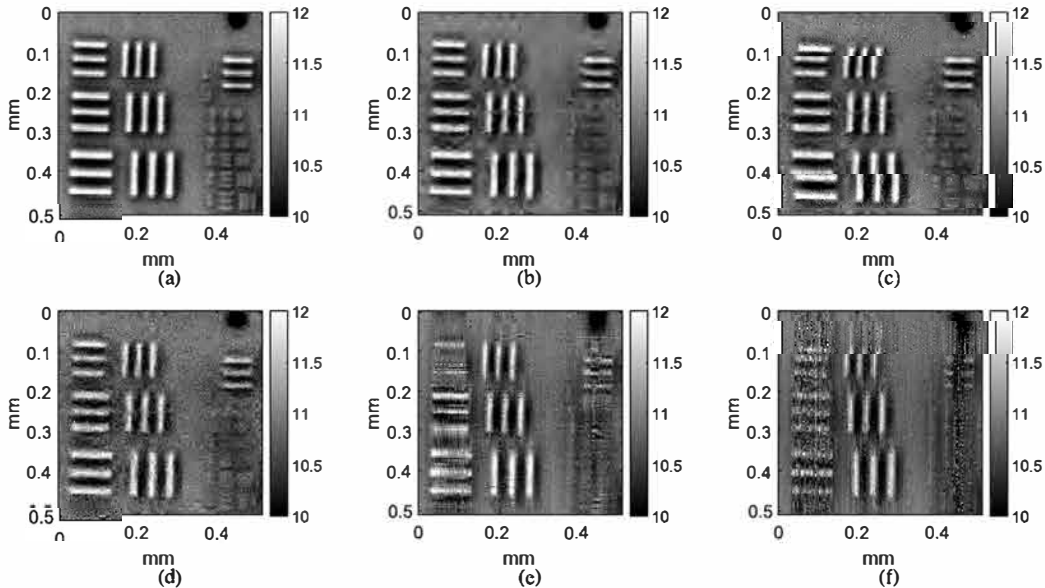


Fig. 5. (a) Fully sampled impedance ( $MRayl$ ) map estimated from RF data acquired on the USAF 1951 resolution test chart, reconstruction results from Gaussian random measurements for a measurement ratio of 0.25 with (b) proposed Cauchy-AMP, (c) ABE-AMP, (d) ST-AMP, (e) IRLS, and (f) L1LS algorithms.

### B. Practical Sensing Patterns for QAM

Theoretically, optimal sensing matrices based on randomness are impractical for QAM data acquisition because RF data are typically acquired continuously as the motor stages are moved. Therefore, this paper investigates three practical sensing schemes, which can be easily implemented using servo motors. The diagonal sensing schemes raster scan oblique lines using a constant predefined angle that is used to vary the measurement rate, that is, a smaller angle leads to denser sampling. The row random sensing pattern is a naive but practical attempt to preserve randomness. Data are also collected using a practical raster scanning approach, but only on randomly selected rows using the random number generator (`rng`) of MATLAB. An input value for `rng` is used to dictate the measurement rate. Finally, the spiral sensing scheme is also a practical sensing scheme that originates in the center of area to be sampled and spreads out following a spiral pattern. The pace of the spreading is parameterized and used to prescribe the measurement rate. For comparison purposes, the spiral

pattern was truncated to cover the same square area as the other two patterns. In actual experiments, the scanned area by the spiral pattern would consist approximately of a circle passing through the four corners of the square.

Fig. 4 illustrates all sensing schemes used to sample data from a target composed of  $256 \times 256$  pixel. A measurement rate of 20% is shown for all three schemes and the white pixels correspond to the area to be spatially sampled.

## IV. SIMULATION RESULTS

Two different sets of experiments have been conducted and results are reported in Sections IV-A and IV-B. The objective of the first set of experiments was to evaluate the performance of the proposed Cauchy-AMP algorithm. The second set of experiments shows the interest of the proposed sampling schemes in QAM and the ability of Cauchy-AMP algorithm to recover high-quality images from the resulting undersampled data. In addition to visual inspection, the peak signal-to-noise ratio (PSNR) and the structural similarity (SSIM) index [32]

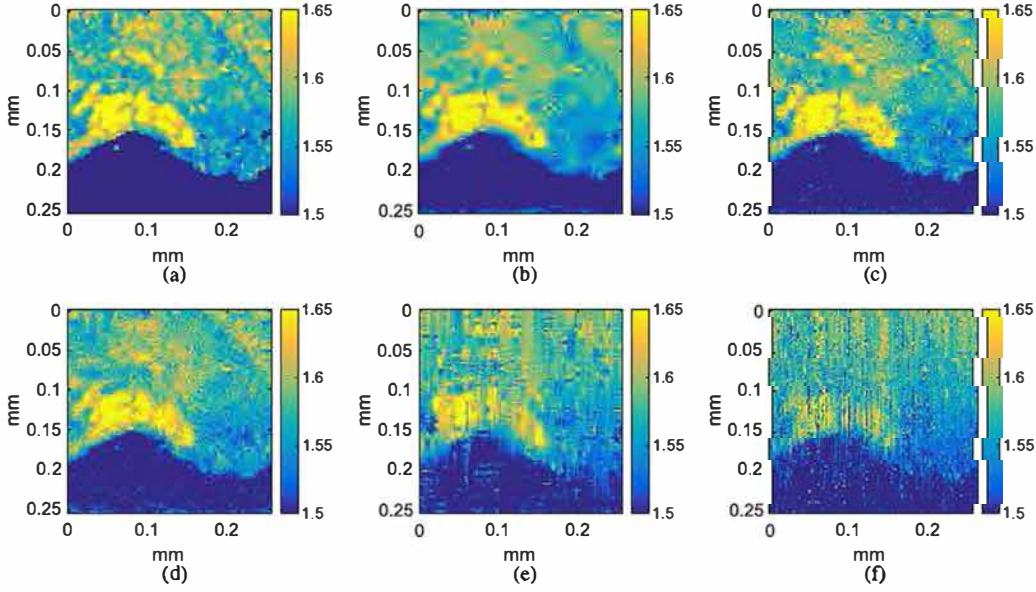


Fig. 6. (a) Human lymph node's fully sampled impedance ( $MRayl$ ) map representing a reconstruction results from Gaussian random measurements for a measurement ratio of 0.25 with (b) proposed Cauchy-AMP, (c) ABE-AMP, (d) ST-AMP, (e) IRLS, and (f) L1LS algorithms.

were used to assess the quality of the reconstructed images by comparing them to the corresponding fully sampled quantitative maps.

#### A. Simulation A: Reconstruction Results With Random Sensing Schemes

The objective of this section is to validate the efficiency of the proposed Cauchy-AMP algorithm in comparison to alternative methods, previously proposed for CS reconstruction. Two of these were described in Section II-C and, while also the AMP-based algorithm, they use ST and ABE as shrinkage functions in (7) and (8). In addition, we also compare to conventional CS reconstruction algorithms, including the L1LS method and the IRLS algorithm for  $l_1$ -norm and  $l_p$  minimization, respectively. These are succinctly outlined in the following.

- 1) *L1LS ( $l_1$ -Regularized Least Squares)*: This  $l_1$ -based algorithm solves an optimization problem of the form

$$\min \|\Phi x - y\|^2 + \lambda \sum_{i=1} |x_i| \quad (18)$$

where  $\lambda$ , a positive number, is a regularisation parameter; in this paper we adopted, by cross validation, 0.01 as the value of  $\lambda$ .

- 2) *IRLS*:

$$\hat{x} = \min_x \|x\|_p \quad \text{s.t. } y = \Phi x. \quad (19)$$

When it comes to estimating a sparse vector characterized by an  $\alpha$ -stable distribution, (19) leads to solving an  $l_p$  minimization problem. Thus, in order to choose the optimum value of  $p$ , we employed the approach described in [30]. This approach was found to be superior to existing  $l_p$  solvers when applied to CS reconstruction of conventional  $B$ -mode images.

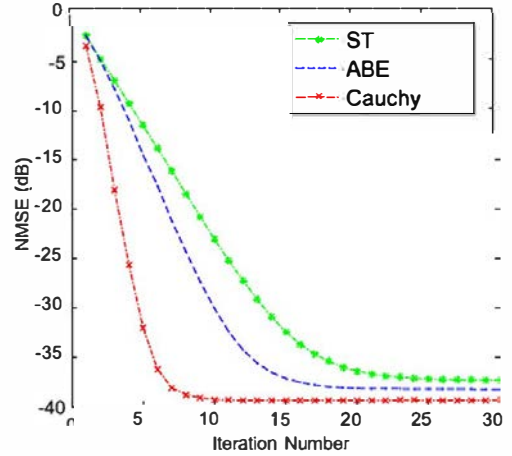


Fig. 7. Comparison of normalized mean squared error (NMSE) according to iteration number for three AMP recovery methods. NMSE values are averaged over 30 simulated QAM images.

The incoherence between the sensing matrix and the sparsifying transform is important in CS applications. Hence, in order to fairly evaluate the performance of the reconstruction algorithms, the results in this section are obtained with two random sensing matrices widely used in the CS literature: image projections on random Gaussian vectors and point-wise multiplication with Bernoulli vectors formed by uniformly random distributed zeros and ones.

Two experimental data volumes were used, from which impedance maps were estimated point-wise using the method in [14]. The first was acquired from a spatial-resolution target consisting of small bars of known width and spacing. Because the chrome used to form those bars is deposited using photolithography, the metal thickness (i.e.,  $\sim 0.12 \mu\text{m}$ ) is much smaller than the wavelength at 250 MHz (i.e.,  $\sim 6 \mu\text{m}$ ); therefore, only an effective acoustic impedance ( $z_{\text{eff}}$ ) can be estimated. The amplitudes of the

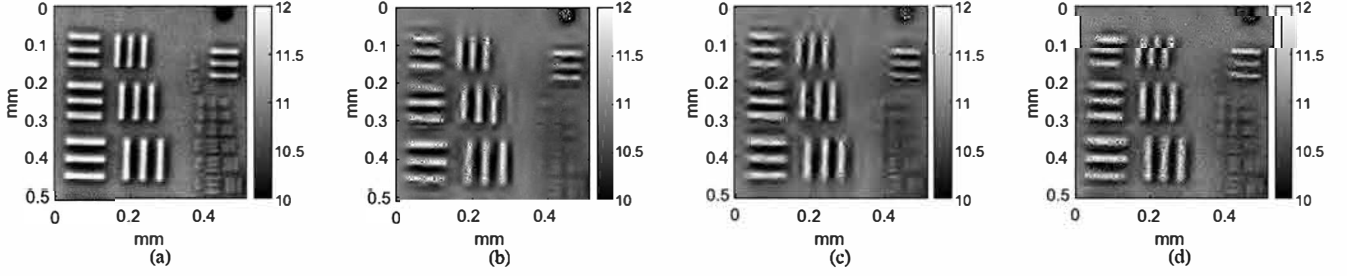


Fig. 8. (a) Fully sampled impedance ( $M Rayl$ ) map estimated from RF data acquired on the USAF 1951 resolution test chart, reconstruction results from Bernoulli random measurements for a measurement ratio of 0.25 with (b) proposed Cauchy-AMP, (c) ABE-AMP, and (d) ST-AMP algorithms.

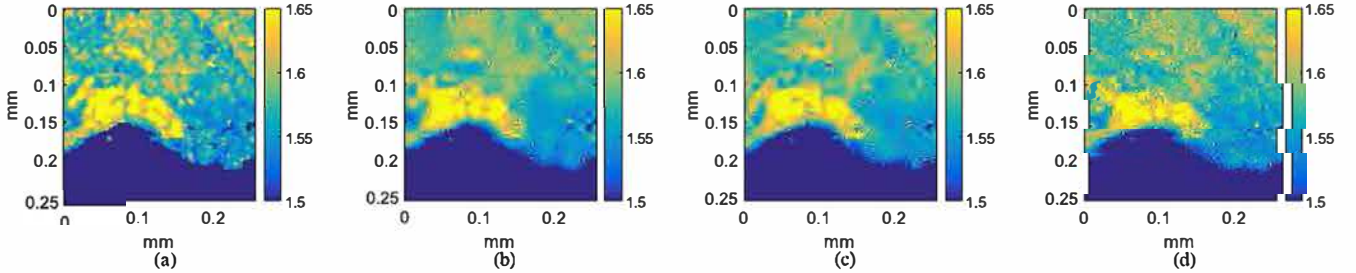


Fig. 9. (a) Fully sampled impedance ( $M Rayl$ ) map representing a reconstruction results from Bernoulli random measurements for a measurement ratio of 0.25 with (b) proposed Cauchy-AMP, (c) ABE-AMP, and (d) ST-AMP algorithms.

TABLE I  
NUMERICAL RESULTS OF RECOVERY QUALITY  
(GAUSSIAN RANDOM SENSING)

Method	SSIM		PSNR (dB)	
	Lymph Node	USAF	Lymph Node	USAF
Cauchy	0.841	0.429	39.08	37.54
ABE	0.811	0.418	39.01	37.45
ST	0.724	0.380	38.41	35.95
IRLS	0.698	0.333	34.97	32.85
LILS	0.457	0.290	32.14	31.30

TABLE II  
COMPARISON OF EXECUTION TIME: THE AVERAGED  
VALUES OVER 30 TRIALS

Method	Runtime (secs)	
	Lymph Node	USAF
Cauchy	3.32	3.47
ABE	2.86	3.00
ST	2.82	2.93
IRLS	62.88	333.61
LILS	4.10	6.88

reflected signal ( $A$ ) and the reference signal ( $B$ ) were used to calculate  $z_{\text{eff}}$  using the following equation from the pressure reflection law [15]:

$$z_{\text{eff}} = z_w \frac{(1 + R_{\text{ref}} \frac{A}{B})}{(1 - R_{\text{ref}} \frac{A}{B})} \quad (20)$$

where  $z_w$  is the known acoustic impedance of water and  $R_{\text{ref}}$  is the pressure reflection coefficient between water and glass slide

$$R_{\text{ref}} = \frac{z_g - z_w}{z_g + z_w} \quad (21)$$

where  $z_g$  is the known acoustic impedance of the glass slide. The second data volume was acquired from a 12- $\mu\text{m}$ -thick section obtained from a lymph node excised from a colorectal cancer patient using the 250-MHz QAM system. For both Gaussian and Bernoulli measurement matrices, the reconstruction results correspond to a measurement rate of 25%, that is, the ratio between the number of CS measurements and the number of pixels in the fully sampled QAM image.

1) *Gaussian Random Measurements*: Figs. 5 and 6 illustrate the impedance images obtained with the five reconstruction algorithms from Gaussian random measurements. It highlights that IRLS and LILS methods severely distorted the fully sampled image compared to the AMP-based algorithms. By closely comparing the AMP-based methods, one may remark that Cauchy-AMP shows a tendency of noise removal with a slightly excessive smoothing effect, whereas ST-AMP and ABE-AMP suffer from several reconstruction artifacts. Table I regroups the PSNR and SSIM values corresponding to the results in Figs. 5 and 6. In addition, Table II provides the runtime of the five methods, averaged over 30 trials. All the algorithms were implemented in MATLAB R2014a environment and executed on a desktop computer equipped with a 2.6 GHz Intel(R) Core™ i7 – 6500C processor with 8 GB RAM.

AMP algorithms outperform the two conventional recovery approaches IRLS and LILS. Particularly, Cauchy-AMP yields the most accurate results compared to its AMP counterparts, at the cost of an execution time marginally higher than ABE- and ST-AMP. The execution time increase per iteration is



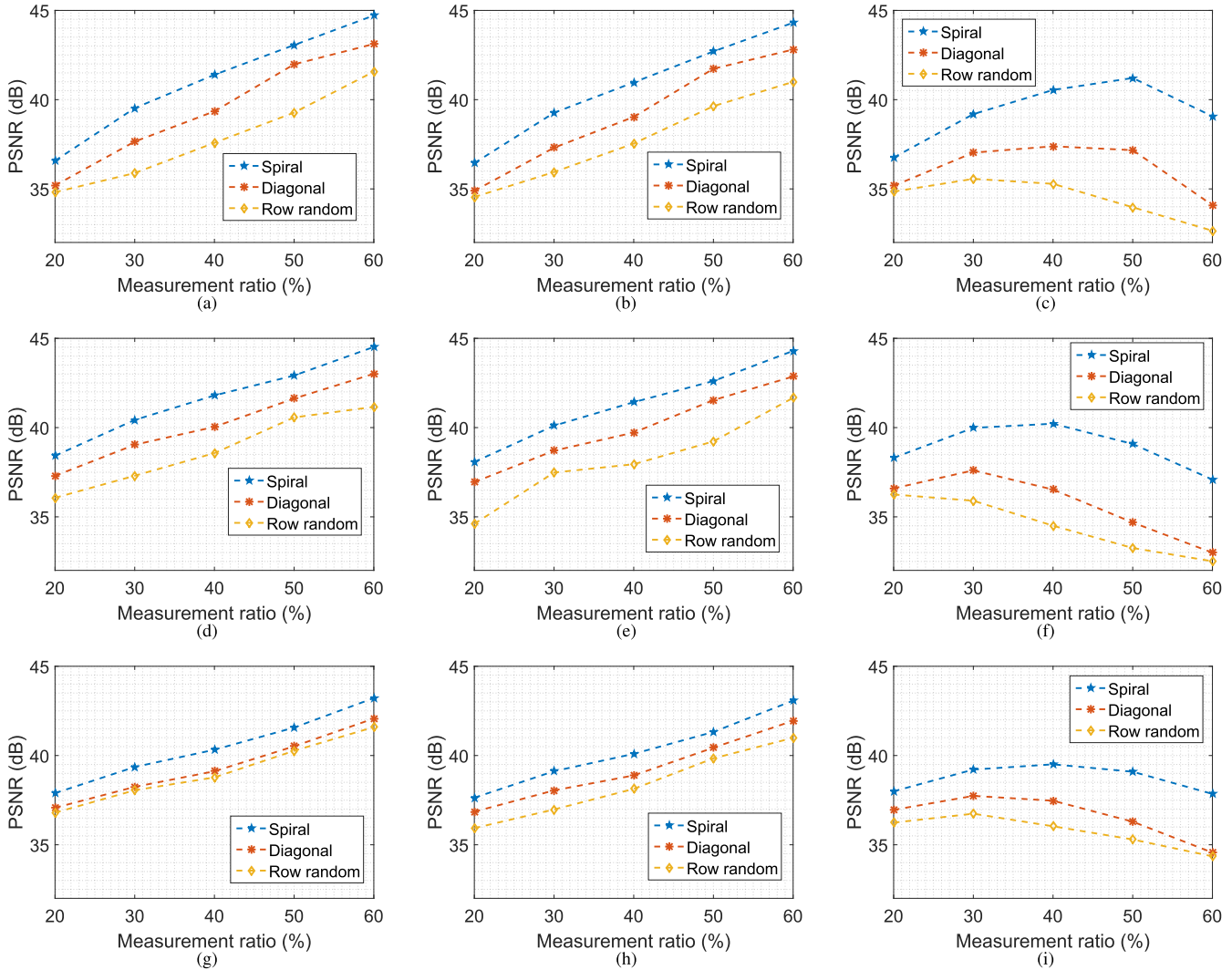


Fig. 10. PSNR results as a function of the measurement rate, the sensing pattern (diagonal, random rows, or spiral), and recovery algorithm (proposed Cauchy-AMP, ABE-AMP, and ST-AMP). (a) Cauchy, (b) ABE, and (c) ST of human cornea at 500 MHz of SoS mode. (d) Cauchy, (e) ABE, and (f) ST of human lymph node at 250 MHz of SoS mode. (g) Cauchy, (h) ABE, and (i) ST of human lymph node at 250 MHz of impedance mode.

explained by the number of parameters to be estimated during the denoising process. Indeed, Cauchy-AMP requires the estimation of an extra parameter compared with ST-AMP and ABE-AMP, that is, the dispersion parameter that determines the spread of the Cauchy distribution. However, the extra computational cost per iteration is significantly mitigated by the faster convergence of Cauchy-AMP as revealed in Fig. 7.

2) *Bernoulli Random Measurements*: The above overall evaluation confirms that AMP-based algorithms are the most promising QAM recovery methods from undersampled data. Nevertheless, measurements obtained by linear projections on Gaussian vectors are not of practical use in QAM. As explained previously, QAM data is acquired point-wise by raster scanning the sample. Thus, Bernoulli random measurements corresponding to random spatial positions are further adapted to QAM acquisition system. Therefore, the three AMP-based methods are tested in this section on the same image used previously but on Bernoulli randomly sampled data. Similar to the previous results,

TABLE III  
NUMERICAL RESULTS OF RECOVERY QUALITY  
(BERNOULLI RANDOM SENSING)

Method	SSIM		PSNR (dB)	
	Lymph Node	USAF	Lymph Node	USAF
Cauchy	0.851	0.424	38.72	34.56
ABE	0.837	0.417	38.56	34.33
ST	0.815	0.415	37.88	34.09

the proposed Cauchy-AMP outperforms the ABE-AMP and ST-AMP algorithms. The three reconstructed images are shown in Figs. 8 and 9. The corresponding quantitative results are regrouped in Table III.

### B. Simulation B: Reconstruction Results With Sensing Schemes Dedicated to QAM

The results shown in the previous section proved the superiority in reconstructing QAM images of the proposed Cauchy-AMP algorithm against four well-established methods. However, Gaussian random measurements are impractical for

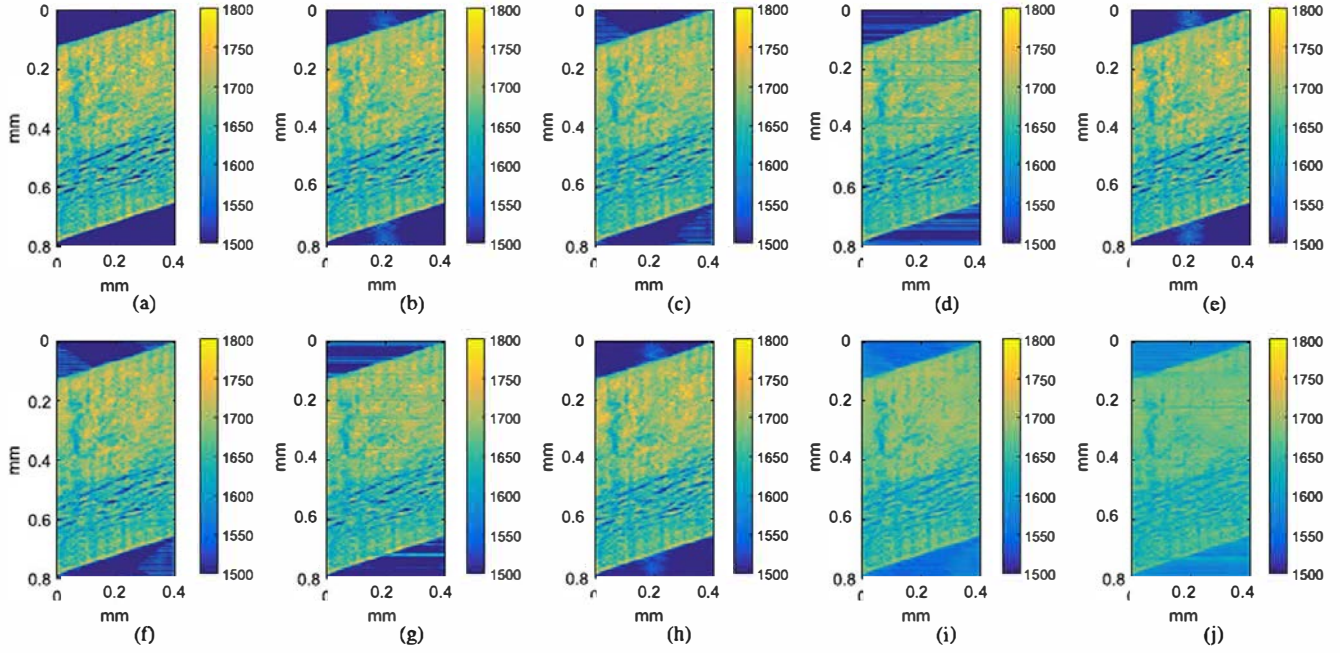


Fig. 11. Reconstruction results of SoS (m/s) map estimated from human cornea data acquired at 500 MHz. (a) Original fully sample data at a pixel resolution of  $1 \mu\text{m}$  per  $1 \mu\text{m}$ . (b)–(d) Reconstructed images with the proposed Cauchy-AMP algorithm for spiral, diagonal, and row random sampling patterns. (e)–(g) Reconstructed images with the ABE-AMP algorithm for the spiral, diagonal, and row random sampling patterns. (h)–(j) Reconstructed images with ST-AMP algorithm for the spiral, diagonal, and row random sampling patterns. All the results correspond to a measurement ratio of 40%.

QAM data acquisition. Similarly and although technically possible, it would be inefficient to move the transducer to transmit and receive ultrasound signals at spatial locations following a Bernoulli random measurements. Therefore, in this second set of simulations, the three AMP-based algorithms are employed to assess the relevance of the practical sensing patterns proposed in this paper (see Section III-B) for QAM imaging.

The simulations used experimental results obtained from three real QAM maps. The first map corresponds to the speed of sound (SoS) map obtained from a human cornea sample using the 500-MHz QAM system. The two other maps are SoS and impedance maps obtained using the 250-MHz QAM system on a human lymph node thin section obtained from a colorectal cancer patient. The fully sampled images correspond to standard raster scanning at conventional spatial scanning frequencies, resulting into a pixel size of  $1 \mu\text{m}$  per  $1 \mu\text{m}$  and respectively of  $2 \mu\text{m}$  per  $2 \mu\text{m}$  for the 500- and 250-MHz data.

All the AMP-algorithm investigations were performed using measurement ratios ranging from 20% to 60% of the data obtained using the conventional raster scanning approach. Fig. 10 displays the resulting PSNR values and permits comparing the QAM image reconstruction quality between the three proposed sensing patterns and the three AMP-based reconstruction algorithms. Blue regions in these images were not included in quantitative analyses because they were devoid of tissues. Independent of the image or algorithm under consideration, results indicate that the spiral pattern always provided the highest PSNR, followed by the diagonal pattern. Figs. 11–13 show the fully sampled images and the ones recovered by the three algorithms from data generated with the three considered patterns for a measurement rate of 40%. Also for the sake of the quantitative

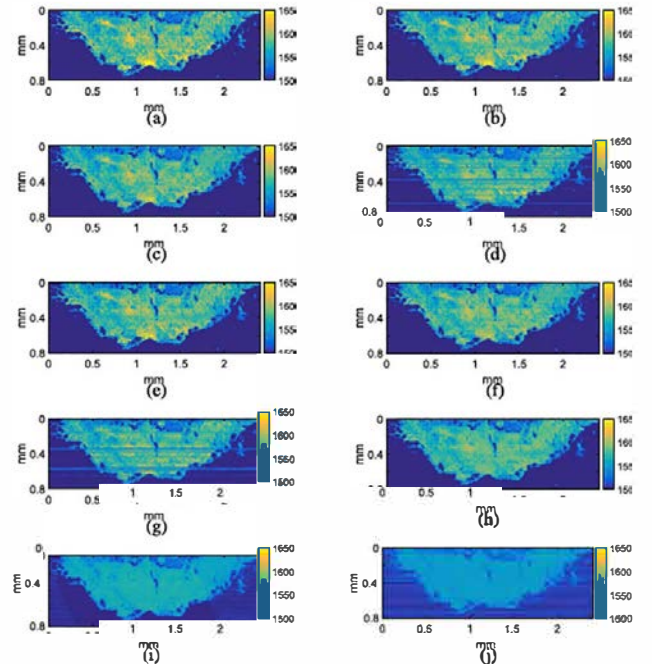


Fig. 12. Reconstruction results of SoS (m/s) map estimated from human lymph node data acquired at 250 MHz. (a) Original fully sample data at a pixel resolution of  $2 \mu\text{m}$  per  $2 \mu\text{m}$ . (b)–(d) Reconstructed images with the proposed Cauchy-AMP algorithm for spiral, diagonal, and row random sampling patterns. (e)–(g) Reconstructed images with ABE-AMP algorithm for spiral, diagonal and row random sampling patterns. (h)–(j) Reconstructed images with ST-AMP algorithm for spiral, diagonal, and row random sampling patterns. All the results correspond to a measurement ratio of 40%.

evaluation corresponding to the figures, the numerical results are in Table IV offered. Overall, visual inspections of these images are consistent with the results shown in Fig. 10, the spiral pattern provides the best result, and the quality of the reconstructions improves with measurement ratio. The

TABLE IV  
NUMERICAL RESULTS OF RECOVERY QUALITY FOR THE RECONSTRUCTED IMAGES SHOWN IN FIGS. 11–13

Image	Method	SSIM			PSNR		
		SPIRAL	DIAGONAL	Y RANDOM	SPIRAL	DIAGONAL	Y RANDOM
Conear 500MHz (SoS)	Cauchy	0.530	0.458	0.415	41.40	39.35	37.58
	ABE	0.509	0.435	0.393	40.97	39.03	37.54
	ST	0.502	0.373	0.306	40.54	37.39	35.28
Lymph Node 250MHz (SoS)	Cauchy	0.445	0.388	0.342	41.80	40.04	38.57
	ABE	0.438	0.374	0.323	41.42	39.72	37.95
	ST	0.418	0.351	0.301	40.22	34.50	36.53
Lymph Node 250MHz (Impedance)	Cauchy	0.911	0.884	0.868	40.32	39.12	38.27
	ABE	0.907	0.878	0.864	40.09	38.89	38.13
	ST	0.896	0.868	0.859	39.51	37.47	36.04

images obtained with a measurement ratio of 40%, that is, Figs. 11–13 illustrate nicely the relative performance of each tested sensing pattern. Fig. 10 reveals that Cauchy denoising provides better PSNR values. The corresponding 2-D maps are shown in Figs. 11–13(b)–(d). The row random pattern results show many artifacts appearing as “transverse” lines. In contrast, the spiral and diagonal sensing patterns do not contain any visually apparent artifacts. In order to determine which of these two sensing patterns performs better for QAM, one can arguably see in Figs. 11–13 that the dense yellow area are better reconstructed using the spiral than the diagonal sensing pattern. This visual assessment is consistent with the quantitative results shown in Fig. 10 and Table IV. Another potential benefit of spiral pattern resides in significantly reduced scanning time. QAM estimation time is typically less important than QAM data acquisition time because tissue properties may change during scanning. Nevertheless, while the proposed AMP approach significantly decreases scanning time, it turns out that it also significantly decreases image formation time, because QAM parameter estimation is done independently on each RF line and is much more time consuming than AMP (see Table II). For example, in the case of the 40% spiral, scanning time is reduced by more than 80% because in conventional raster scanning most of the time is spent accelerating and decelerating in each scan line, whereas the spiral is a smooth continuous curve that can be scanned at almost constant speed with servo motors. In addition, initial parameter estimation time is also reduced by 60% prior to the application of the AMP algorithm. The raster scanning and parameter estimation times for the lymph node example (Figs. 12 and 13) were approximately 20 and 15 min. The 40% spiral AMP approach would reduce these times to approximately 4 and 8 min. In conclusion, these sets of simulations reveal that combining a spiral sensing pattern with a measurement ratio of 40%, and a Cauchy-AMP recovery is the best compromise between a practical spatial sampling pattern easily implementable with servo motors and image reconstruction quality for QAM imaging.

However, in three graphs (right column) corresponding to ST-AMP of Fig. 10, intractable problems are found. To date researches associated with CS recovery normally have been reporting that the relationship between recovery quality and measurement ratio is a monotonically increase or decrease within usually simulated range. By contrast, ST-AMP shows unfamiliar results. Indeed CS has been constructed on the

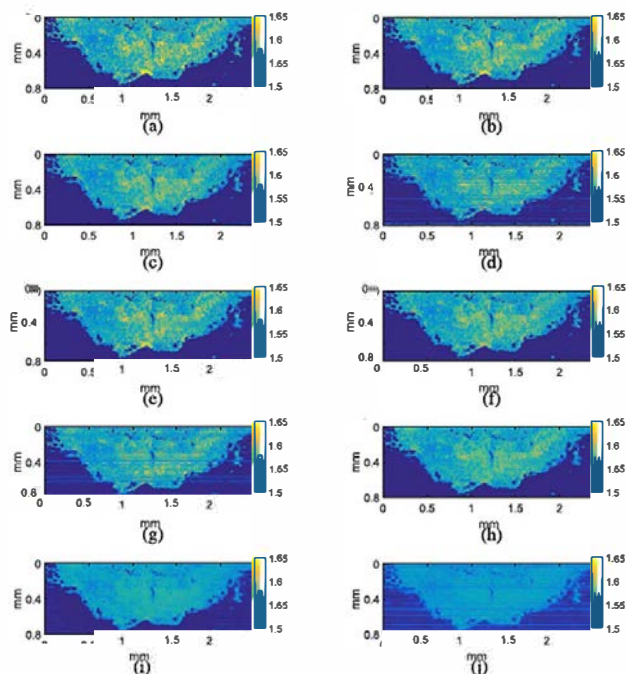


Fig. 13. Reconstruction results of impedance ( $M Rayl$ ) map estimated from human lymph node data acquired at 250 MHz. (a) Original fully sample data at a pixel resolution of  $2 \mu m$  per  $2 \mu m$ . (b)–(d) Reconstructed images with the proposed Cauchy-AMP algorithm for spiral, diagonal, and row random sampling patterns. (e)–(g) Reconstructed images with ABE-AMP algorithm for spiral, diagonal, and row random sampling patterns. (h)–(j) Reconstructed images with ST-AMP algorithm for spiral, diagonal, and row random sampling patterns. All the results correspond to a measurement ratio of 40%.

premise of sensing matrices satisfying mathematical completeness such as restricted isometry property and incoherence to ensure perfect recovery of sparse signals. Nevertheless, since this paper prioritized the aspect of practical implementation of sensing strategy, the proposed sensing patterns unavoidably followed deterministic sensing trajectories rather than randomness dominating CS sensing arena owing to meeting essential conditions stated above [34]. From this perspective, further study will focus on the development of practical sensing schemes retaining the pertinent properties of random matrices [35].

## V. CONCLUSION

In this paper, we introduced a new framework for compressive sampling reconstruction of QAM images together

with associated sampling patterns. We proposed and tested three compressive sampling measurement matrices, with a view of reducing both acquisition time and the amount of samples required, while taking into account the constraints imposed by the design of current experimental QAM systems. Specifically, we assessed the relative merits of diagonal sampling, row random sampling, and spiral scanning as underlying patterns in designing a CS measurement matrix. We adopted an AMP strategy for the image reconstruction component of our framework, owing to its similarity to  $l_p$  minimization. In particular, in the multiscale wavelet domain, we employed a Cauchy-based MAP estimation algorithm to perform the image denoising step required by an AMP algorithm.

We tested our methods in comparison with various compressive image reconstruction algorithms, when applied to QAM data. Our results showed improved performance both with respect to alternative AMP techniques that use different denoising strategies as well as to other, more standard, approaches to CS reconstruction, which employ  $l_1$ -norm, or  $l_p$  minimization.

The results of this paper could prove invaluable in QAM imaging. CS has the potential to yield significantly improved scan times, smaller data sets, faster image formation without degrading image quality. Moreover, CS approaches would reduce experimental challenges currently encountered in QAM imaging. For example, the spiral sampling approach could be implemented on cheap, potentially less precise, servo motors. In addition, reducing scan time would reduce changes that the tissue properties may suffer during scan and would limit temperature variations, particularly in the coupling medium, which can greatly effect speed of sound estimates. Therefore, CS approaches could potentially bring about a new generation of QAM systems that would be lower in costs and simpler to use. Finally, the study of dominant factors having an effect on the convergence rate of the proposed method is definitely an interesting study that will be part of our future work.

#### ACKNOWLEDGMENT

The authors would like to thank Dr. D. Rohrbach for his help with the acquisition and processing of the experimental data.

#### REFERENCES

- [1] M. F. Marmor, H. K. Wickramasinghe, and R. A. Lemons, "Acoustic microscopy of the human retina and pigment epithelium," *Invest. Ophthalmol. Vis. Sci.*, vol. 16, no. 7, pp. 660–666, Jul. 1977.
- [2] D. Rohrbach, H. O. Lloyd, R. H. Silverman, and J. Mamou, "High-resolution maps of acoustic properties at 250 MHz of unstained fixed murine retinal layers," *J. Acoust. Soc. Amer.*, vol. 137, no. 5, pp. EL381–EL387, May 2015.
- [3] S. Irie *et al.*, "Speed of sound in diseased liver observed by scanning acoustic microscopy with 80 MHz and 250 MHz," *J. Acoust. Soc. Amer.*, vol. 139, no. 1, pp. 512–519, Jan. 2016.
- [4] J. A. Hildebrand, D. Rugar, R. N. Johnston, and C. F. Quate, "Acoustic microscopy of living cells," *Proc. Nat. Acad. Sci. USA*, vol. 78, no. 3, pp. 1656–1660, Mar. 1981.
- [5] J. Mamou, D. Rohrbach, E. Saegusa-Beecroft, E. Yanagihara, J. Machi, and E. J. Feleppa, "Ultrasound-scattering models based on quantitative acoustic microscopy of fresh samples and unstained fixed sections from cancerous human lymph nodes," in *Proc. IEEE Int. Ultrason. Symp. (IUS)*, Taipei, Taiwan, Oct. 2015, pp. 1–4.

- [6] K. Dabov, A. Foi, V. Katkovnik, and K. Egiazarian, "Image denoising by sparse 3-D transform-domain collaborative filtering," *IEEE Trans. Image Process.*, vol. 16, no. 8, pp. 2080–2095, Aug. 2007.
- [7] M. Unser, P. D. Tafti, and Q. Sun, "A unified formulation of Gaussian versus sparse stochastic processes—Part I: Continuous-domain theory," *IEEE Trans. Inf. Theory*, vol. 60, no. 3, pp. 1945–1962, Mar. 2014.
- [8] E. J. Candès, J. Romberg, and T. Tao, "Robust uncertainty principles: Exact signal reconstruction from highly incomplete frequency information," *IEEE Trans. Inf. Theory*, vol. 52, no. 2, pp. 489–509, Feb. 2006.
- [9] D. L. Donoho, A. Maleki, and A. Montanari, "Message-passing algorithms for compressed sensing," *Proc. Nat. Acad. Sci. USA*, vol. 106, no. 45, pp. 18914–18919, Nov. 2009.
- [10] J. Tan, Y. Ma, and D. Baron, "Compressive imaging via approximate message passing with image denoising," *IEEE Trans. Signal Process.*, vol. 63, no. 8, pp. 2085–2092, Apr. 2015.
- [11] P. R. Hill, J.-H. Kim, A. Basarab, D. Kouame, D. R. Bull, and A. Achim, "Compressive imaging using approximate message passing and a Cauchy prior in the wavelet domain," in *Proc. IEEE Int. Conf. Image Process. (ICIP)*, Phoenix, AZ, USA, Sep. 2016, pp. 2514–2518.
- [12] J. Ilow and D. Hatzinakos, "Analytic alpha-stable noise modeling in a Poisson field of interferers or scatterers," *IEEE Trans. Signal Process.*, vol. 46, no. 6, pp. 1601–1611, Jun. 1998.
- [13] T. Chernyakova and Y. C. Eldar, "Fourier-domain beamforming: The path to compressed ultrasound imaging," *IEEE Trans. Ultrason., Ferroelect., Freq. Control*, vol. 61, no. 8, pp. 1252–1267, Aug. 2014.
- [14] D. Rohrbach, A. Jakob, H. O. Lloyd, S. H. Tretbar, R. H. Silverman, and J. Mamou, "A novel quantitative 500-MHz acoustic microscopy system for ophthalmologic tissues," *IEEE Trans. Biomed. Eng.*, vol. 64, no. 3, pp. 715–724, May 2016.
- [15] L. E. Kinsler, A. R. Frey, A. B. Coppens, and J. V. Sanders, *Fundamentals of Acoustics*, 4th ed. New York, NY, USA: Wiley, 2000.
- [16] D. L. Donoho, "Compressed sensing," *IEEE Trans. Inf. Theory*, vol. 52, no. 4, pp. 1289–1306, Apr. 2006.
- [17] R. Chartrand and W. Yin, "Iteratively reweighted algorithms for compressive sensing," in *Proc. IEEE Int. Conf. Acoust., Speech Signal Process. (ICASSP)*, Apr. 2008, pp. 3869–3872.
- [18] J. A. Tropp and A. C. Gilbert, "Signal recovery from random measurements via orthogonal matching pursuit," *IEEE Trans. Inf. Theory*, vol. 53, no. 12, pp. 4655–4666, Dec. 2007.
- [19] T. Blumensath and M. E. Davies, "Iterative hard thresholding for compressed sensing," *Appl. Comput. Harmon. Anal.*, vol. 27, no. 3, pp. 265–274, Nov. 2009.
- [20] D. L. Donoho, "De-noising by soft-thresholding," *IEEE Trans. Inf. Theory*, vol. 41, no. 3, pp. 613–627, May 1995.
- [21] C. A. Metzler, A. Maleki, and R. G. Baraniuk. (2014). "From denoising to compressed sensing." [Online]. Available: <https://arxiv.org/abs/1406.4175>
- [22] A. Achim, A. Bezerianos, and P. Tsakalides, "Novel Bayesian multiscale method for speckle removal in medical ultrasound images," *IEEE Trans. Med. Imag.*, vol. 20, no. 8, pp. 772–783, Aug. 2001.
- [23] A. Achim and E. E. Kuruoglu, "Image denoising using bivariate  $\alpha$ -stable distributions in the complex wavelet domain," *IEEE Signal Process. Lett.*, vol. 12, no. 1, pp. 17–20, Jan. 2005.
- [24] M. A. T. Figueiredo and R. D. Nowak, "Wavelet-based image estimation: An empirical Bayes approach using Jeffrey's noninformative prior," *IEEE Trans. Image Process.*, vol. 10, no. 9, pp. 1322–1331, Sep. 2001.
- [25] M. A. Kutay, A. P. Petropulu, and C. W. Piccoli, "On modeling biomedical ultrasound RF echoes using a power-law shot-noise model," *IEEE Trans. Ultrason., Ferroelect., Freq. Control*, vol. 48, no. 4, pp. 953–968, Jul. 2001.
- [26] A. P. Petropulu, J. C. Pesquet, and X. Yang, "Power-law shot noise and its relationship to long-memory alpha-stable processes," *IEEE Trans. Signal Process.*, vol. 48, no. 7, pp. 1883–1892, Jul. 2000.
- [27] D. L. Donoho and J. M. Johnstone, "Ideal spatial adaptation by wavelet shrinkage," *Biometrika*, vol. 81, no. 3, pp. 425–455, 1994.
- [28] D. L. Donoho, A. Maleki, and A. Montanari, "How to design message passing algorithms for compressed sensing," to be published.
- [29] J. H. Kim, A. Basarab, P. R. Hill, D. R. Bull, D. Kouamé, and A. Achim, "Ultrasound image reconstruction from compressed measurements using approximate message passing," in *Proc. Eur. Signal Process. Conf. (EUSIPCO)*, Aug. 2016, pp. 557–561.
- [30] A. Achim, B. Buxton, G. Tzagkarakis, and P. Tsakalides, "Compressive sensing for ultrasound RF echoes using  $\alpha$ -stable distribution," in *Proc. Annu. Int. Conf. IEEE Eng. Med. Biol. (EMBC)*, Buenos Aires, Argentina, Aug. 2010, pp. 4304–4307.

- [31] S. S. Chen, D. L. Donoho, and M. A. Saunders, "Atomic decomposition by basis pursuit," *SIAM J. Sci. Comput.*, vol. 20, no. 1, pp. 33–61, 1999.
- [32] Z. Wang, A. C. Bovik, H. R. Sheikh, and E. P. Simoncelli, "Image quality assessment: From error visibility to structural similarity," *IEEE Trans. Image Process.*, vol. 13, no. 4, pp. 600–612, Apr. 2004.
- [33] E. Candès and J. Romberg, "Sparsity and incoherence in compressive sampling," *Inverse Problems*, vol. 23, no. 3, p. 969, 2007.
- [34] J. C. Emmanuel and W. B. Michael, "An introduction to compressive sampling," *IEEE Signal Process. Mag.*, vol. 25, no. 2, pp. 21–30, Mar. 2008.
- [35] G. Kutyniok, "Theory and applications of compressed sensing," *GAMM-Mitteilungen*, vol. 36, no. 1, pp. 79–101, Aug. 2013.



**Jonghoon Kim** received the master's degree in biomedical engineering from the University of Bristol, Bristol, U.K., in 2016, where he is currently pursuing the Ph.D. degree with the Visual Information Laboratory.

His current research interests include inverse problem, sparsity approaches, and sampling theory with application to reconstruction of quantitative acoustic microscopy images.



**Jonathan Mamou** (S'03–M'05–SM'11) received the B.S. degree from the Ecole Nationale Supérieure des Télécommunications, Paris, France, in 2000. He received the M.S. and Ph.D. degrees in electrical and computer engineering from the University of Illinois at Urbana–Champaign, Urbana, IL, USA, in 2002 and 2005, respectively.

He is currently a Research Manager with the F. L. Lizzi Center for Biomedical Engineering, Riverside Research, New York, NY, USA. He is the Co-Editor of the book *Quantitative Ultrasound in Soft Tissues* (Springer, 2013). His current research interests include the theoretical aspects of ultrasonic scattering, ultrasonic medical imaging, ultrasound contrast agents, and biomedical image processing.

Dr. Mamou is a fellow of the American Institute of Ultrasound in Medicine (AIUM) and a member of the Acoustical Society of America. He served as the Chair of the AIUM High-Frequency Clinical and Preclinical Imaging Community of Practice. He is an Associate Editor of *Ultrasonic Imaging* and the *IEEE TRANSACTIONS ON ULTRASONICS, FERROELECTRICS, AND FREQUENCY CONTROL* and a reviewer for numerous journals.



**Paul R. Hill** (M'12) received the B.Sc. degree from Open University, U.K., in 1996, and the M.Sc. degree and the Ph.D. degree in image segmentation and fusion from the University of Bristol, Bristol, U.K., in 1998 and 2002, respectively.

He is currently a Senior Research Fellow with the Department of Electrical and Electronic Engineering, University of Bristol, where he is also a Lecturer in audio technology. His current research interests include image and video analysis, compression, and fusion.



**Nishan Canagarajah** received the B.A. (Hons.) and Ph.D. degrees in DSP techniques for speech enhancement from the University of Cambridge, Cambridge, U.K.

He is currently a Professor of multimedia signal processing with the University of Bristol, Bristol, U.K. He has authored over 300 papers and two books. His current research interests include image and video coding, image segmentation, content-based video retrieval, 3-D video, and image fusion. He is widely supported in these areas by industry, EU, and the EPSRC.



**Denis Kouamé** (M'97) received the Ph.D. and Habilitation à Diriger des Recherches degrees in signal processing and medical ultrasound imaging from the University of Tours, Tours, France, in 1996 and 2004, respectively.

From 1996 to 1998, he was a Senior Engineer with GIP Tours, Tours. From 1998 to 2008, he was an Assistant and then an Associate Professor with the University of Tours, where he was the Head of the Signal and Image Processing Group from 2000 to 2006, and then the Head of the Ultrasound Imaging Group from 2006 to 2008 with the Ultrasound and Signal Laboratory. He currently leads the Image Comprehension and Processing Group, Institut de Recherche en Informatique de Toulouse (IRIT), Toulouse, France. He is currently a Professor with the Paul Sabatier University of Toulouse, Toulouse, and a member of the IRIT Laboratory. His current research interests include signal and image processing with applications to medical imaging and particularly ultrasound imaging, including high-resolution imaging, image resolution enhancement, Doppler signal processing, detection and estimation with application to cerebral emboli detection, multidimensional parametric modeling, spectral analysis, and inverse problems related to compressed sensing and restoration.

Dr. Kouamé has been involved in the organization of several conferences. He has also led a number of invited conferences, special sessions, and tutorials at several IEEE conferences and workshops. He has been an Associate Editor of the *IEEE TRANSACTIONS ON ULTRASONICS, FERROELECTRICS, AND FREQUENCY CONTROL* and the *IEEE TRANSACTIONS ON IMAGE PROCESSING*.



**Adrian Basarab** (S'05–M'08) received the M.S. and Ph.D. degrees in signal and image processing from the National Institute for Applied Sciences of Lyon, Lyon, France, in 2005 and 2008, respectively.

Since 2009, he has been an Associate Professor with University Paul Sabatier Toulouse 3, Toulouse, France, and a member of the IRIT Laboratory (UMR CNRS 5505), Toulouse. His current research interests include medical imaging, and more particularly motion estimation, inverse problems, and ultrasound image formation.

Dr. Basarab is currently an Associate Editor of *Digital Signal Processing*.



**Alin Achim** (S'99–M'03–SM'09) received the M.Eng. and M.Sc. degrees in electrical engineering from the University Politehnica of Bucharest, Bucharest, Romania, in 1995 and 1996, respectively, and the Ph.D. degree in biomedical engineering from the University of Patras, Patras, Greece, in 2003.

He obtained an ERCIM (European Research Consortium for Informatics and Mathematics) postdoctoral fellowship which he spent with the Institute of Information Science and Technologies (ISTI-CNR), Pisa, Italy and with the French National Institute

for Research in Computer Science and Control (INRIA), Sophia Antipolis, France. He was with the Department of Electrical & Electronic Engineering, University of Bristol, Bristol, U.K., as a Lecturer in 2004 and as a Senior Lecturer (Associate Professor) in 2010, where he is currently a Reader in biomedical image computing. He has coauthored over 100 scientific publications, including more than 30 journal papers. His current research interests include statistical signal, image and video processing with particular emphasis on the use of sparse distributions within sparse domains.

Dr. Achim is an elected member of the Bio Imaging and Signal Processing Technical Committee, IEEE Signal Processing Society, and an affiliated member of the Signal Processing Theory and Methods Technical Committee, IEEE Signal Processing Society. He is a member of the IET. He is an Associate Editor of the *IEEE TRANSACTIONS ON IMAGE PROCESSING*.